



Research paper

Effect of the calcination temperature on the visible light photocatalytic activity of direct contact Z-scheme $\text{g-C}_3\text{N}_4\text{-TiO}_2$ heterojunction

Juan Li ^{a,b}, Min Zhang ^a, Xuan Li ^a, Qiuye Li ^{a,*}, Jianjun Yang ^{a,*}

^a National & Local Joint Engineering Research Center for Applied Technology of Hybrid Nanomaterials, Collaborative Innovation Center of Nano Functional Materials and Applications of Henan Province, Henan University, Kaifeng, 475004, China

^b Henan Engineering Research Center of Resource & Energy Recovery from Waste, Henan University, Kaifeng, 475004, China

ARTICLE INFO

Article history:

Received 2 March 2017

Received in revised form 19 April 2017

Accepted 24 April 2017

Available online 27 April 2017

ABSTRACT

Z-scheme $\text{g-C}_3\text{N}_4\text{-TiO}_2$ heterojunctions containing $\text{g-C}_3\text{N}_4$ nanosheets with different thickness were prepared by sintering the mixture of $\text{g-C}_3\text{N}_4$ and nanotube titanic acid (denoted as NTA) at different temperatures in air. As-prepared Z-scheme $\text{g-C}_3\text{N}_4\text{-TiO}_2$ heterojunctions were characterized by X-ray diffraction, transmission electron microscopy, atomic force microscopy, X-ray photoelectron spectroscopy, ultraviolet-visible light diffuse reflectance spectrometry, electron spin resonance, and photoluminescence spectrometry. Findings indicate that the annealing temperature has crucial effects on the visible-light photocatalytic activity ($\lambda \geq 420 \text{ nm}$) of the as-prepared Z-scheme $\text{g-C}_3\text{N}_4\text{-TiO}_2$ heterojunctions. The Ti^{3+} and porous $\text{g-C}_3\text{N}_4$ nanosheets formed upon the calcination at 600°C as well as the low concentration of bulk single-electron trapped oxygen vacancy are favorable to the transport of the photoexcited charge carriers. This, in association with the Z-scheme system, contributes to improving the photocatalytic activity of $\text{g-C}_3\text{N}_4\text{-TiO}_2$ photocatalysts. As a result, $\text{g-C}_3\text{N}_4\text{-TiO}_2$ photocatalyst prepared at 600°C exhibits good photocatalytic activity towards the degradation of propylene and hydrogen generation by water-splitting under visible light irradiation.

© 2017 Elsevier B.V. All rights reserved.

1. Introduction

As the well known photocatalyst, anatase TiO_2 has been investigated extensively due to its good stability, low cost and strong oxidation ability [1]. However, anatase TiO_2 with a wide band-gap needs to be excited by ultraviolet, while its high photoinduced electron-hole recombination rate is harmful to photocatalytic activity. The two defects seriously confined its practical application in environmental governance [2]. To improve its visible light absorption and activity, metal doping [3,4], non-metal doping [5–7], metal and nonmetal codoping [8,9] as well as Ti^{3+} and oxygen vacancy self-doped [10–12] were all the effective methods. Unfortunately, metal doping especially noble metal doping is often less cost-effective, while non-metal doping is usually less efficient in increasing the photocatalytic activity of TiO_2 . Moreover, although the method of metal and nonmetal codoping can

effectively improve activity, but there still exists the problem of preparation process complex and high cost. So coupling TiO_2 with other narrow band-gap semiconductors is found to be an efficient way [13–15].

In recent years, graphite-phase carbon nitride ($\text{g-C}_3\text{N}_4$) has acquired highly concern of many researchers in the world on account of the unique two-dimensional planar structure, high physicochemical stability, easy synthesis, low cost and the relatively narrow band-gap (2.7 eV), and has been widely used for hydrogen generation by water-splitting [16], CO_2 reduction [17] or organic pollutant degradation [18] under visible light irradiation. Nevertheless, single bulk $\text{g-C}_3\text{N}_4$ currently has very low activity due to its high photogenerated electrons-holes recombination efficiency and small specific surface area [19,20]. To deal with these issues, some researchers tried to combine bulk $\text{g-C}_3\text{N}_4$ with semiconductor materials, thereby obtaining thin $\text{g-C}_3\text{N}_4$ nanosheets with improved visible light utilization efficiency [21–24]. Especially, due to its non-toxic, stabilization, metal-free and excellent visible absorption ability, $\text{g-C}_3\text{N}_4$ could be used as a good photosensitizer to enhance the visible light activity of the wide band-gap semiconductor such as TiO_2 [13–15,25–29]. However, most of

* Corresponding authors.

E-mail addresses: qiuyeli@henu.edu.cn (Q. Li), yangjianjun@henu.edu.cn (J. Yang).

these studies mainly focused on the building of heterojunction (traditional [21,22] or Z scheme [17,18,23]) between the appropriate energy band materials and there was little research to study the influence of the g-C₃N₄ structure itself in the composites to the photocatalysis. In fact, the thickness and porosity of g-C₃N₄ nanosheets had important impact to the light absorption, charge carriers transport efficiency and specific surface area and then would further affect the photocatalysis activity. Niu et al. [30] prepared the remarkably improved photocatalytic activities of g-C₃N₄ nanosheets with a thickness of around 2 nm by thermal oxidation etching of bulk g-C₃N₄ in air. Yang et al. [31] and Lin et al. [32] separately employed liquid phase solvents exfoliation bulk g-C₃N₄ to prepare the few-layered or monolayer g-C₃N₄ nanosheets which both displayed the enhanced visible light photocatalytic activities.

In this article, we select g-C₃N₄ to modify the novel-TiO₂ (obtained by the dehydration of nanotube titanic acid (denoted as NTA)) possessing a certain degree of visible light absorption and a large amount of single-electron-trapped oxygen vacancy, hoping to construct Z-scheme g-C₃N₄-TiO₂ heterojunction photocatalysts by simple solid sintering method. Due to the fact that the photocatalytic activity of the obtained composites with different heating temperatures had the considerable difference, we discussed the effect of the annealing temperature to the band structure, the thickness of g-C₃N₄ nanosheets, optical absorption and charge carriers transport performance of the nanocomposites in detail by systematic characterization and proposed the possible mechanism.

2. Experimental

2.1. Materials and methods

All the raw materials were analytical reagent and did not make any further treatment. The details about the preparation of NTA, bulk g-C₃N₄, g-C₃N₄ nanosheets and g-C₃N₄-TiO₂ composites are available in our previous published work [33]. Namely, NTA was prepared by TiO₂ (P25) in the concentrated alkaline hydrothermal treatment for 24 h at 150 °C while the samples of bulk g-C₃N₄, g-C₃N₄ nanosheets and x%g-C₃N₄-TiO₂-y composites (x denoted the mass percentage of g-C₃N₄ in the mixture of bulk g-C₃N₄ and NTA and y represented the calcination temperature) were obtained by simple high temperature calcination in air. Specifically, bulk g-C₃N₄ was prepared by calcining melamine at 550 °C for 2 h, and g-C₃N₄ nanosheets was acquired by heating the bulk g-C₃N₄ at 600 °C for 2 h in air.

2.2. Characterization

The crystal structure of the photocatalysts were confirmed by X-ray diffractometer (XRD, Bruker D8-ADVANCE, Germany; Cu-K_α radiation ($\lambda = 0.15418 \text{ nm}$), 40 kV and 40 mA). The morphology of the samples was obtained by transmission electron microscopy (TEM, JEOL JEM-2100, Japan) and an atomic force microscope (AFM, Bruker Dimension Icon, Germany). The BET (Brunauer, Emmett and Teller) specific surface area was determined by nitrogen adsorption-desorption isotherms (Quadasorb SI instrument, USA). The thermal stability of g-C₃N₄-TiO₂ photocatalysts in the temperature range of 25–1000 °C was evaluated by thermogravimetric analysis (TGA; SDTA 851e, Switzerland) at a heating rate of 10 °C min⁻¹ in air. X-ray photoelectron spectroscopy (XPS) test was carried out on a Thermo ESCALAB 250Xi spectrometer (USA; the binding energy of contaminant carbon (284.8 eV) was used as the reference). The UV-vis diffuse reflection spectra were recorded on a Shimadzu UV-2600 UV/Vis spectrophotometer (Japan; BaSO₄ as reference sample). Electron spin resonance (ESR) spectra were tested on a spectrometer (Bruker EMX-10/12,

Germany) with a 100 kHz field modulation, a 1.0 G amplitude modulation and a 20.4 mW microwave power at room temperature in air. The fluorescence emission spectra were measured on the F-7000 FL spectrophotometer with the excitation wavelength of 315 nm. The time-resolved fluorescence decay spectra were studied by an FLS980 fluorescence spectrophotometer (295 nm laser excitation, England).

2.3. Photocatalytic activity tests and photoelectrochemical measurements

The photocatalytic activity was evaluated by monitoring the oxidation of propylene oxidation under visible light irradiation [33,34]. The light source was a 300 W xenon lamp (PLS-SXE300/300UV) with a 420 nm cutoff filter ($\lambda \geq 420 \text{ nm}$). The degradation rate of propylene was calculated according to the change of concentration for C₃H₆ before and after visible light illumination which was detected by a gas chromatograph (Shimadzu GC-9A, Japan) equipped with a flame ionization detector.

The photocurrent-time curve was measured by an electrochemical workstation (CHI600E China; a standard three-electrode photoelectrochemical cell with 0.1 M Na₂SO₄ solution as the electrolyte was adopted) under the periodic illumination at a definite time interval. About 20 mg sample was first put into 0.5 mL of ethanol and ultrasonic dispersed for 20 min. Then the paste was coated onto the conducting glass and dried at 120 °C for 3 h in the oven. Lastly, the conducting glass with coated samples and platinum wire were used as working and counter electrodes respectively and a saturated calomel electrode (SCE) was used as the reference electrode. Before measurement the electrolyte was purged by inletting argon for 20 min to get rid of the dissolved oxygen. The light source was the same as the photocatalytic activity measurement.

3. Results and discussion

3.1. The photocatalytic activity

To investigate the influence of the annealing temperature to the composites photocatalytic activity, we prepared a series of 20%g-C₃N₄-TiO₂ composites under different temperatures. As seen from Fig. 1A, the photocatalytic activity of 20%g-C₃N₄-TiO₂ composites tend to rise initially and decrease later with elevating calcination temperatures. Especially, 20%g-C₃N₄-TiO₂-400 and 20%g-C₃N₄-TiO₂-500 exhibit similar low photocatalytic activity, while 20%g-C₃N₄-TiO₂-600 exhibits the best photocatalytic activity. The reason could be that g-C₃N₄ was very stable below 600 °C, but it would partially decompose to form thin g-C₃N₄ nanosheets in air at 600 °C [33]. Moreover, NTA would dehydrate to form novel anatase TiO₂ which contained large amounts of single-electron-trapped oxygen vacancy (denoted as V_o[•]) when the temperature exceeded 300 °C [35]. So the sample of 300 °C had the poor crystallinity (seen in Fig. 2B) for the incomplete dehydration which resulted in the very low photoactivity. According to Fig. S3 in the supporting information, g-C₃N₄ would almost decompose completely at 700 °C and Fig. 2B indicated that rutile TiO₂ appeared in the sample of 20%g-C₃N₄-TiO₂-700 which usually had very poor photoactivity.

So we respectively selected 400 °C (g-C₃N₄ stable exists) and 600 °C (g-C₃N₄ partially decomposes) as the annealing temperature to study the effect of g-C₃N₄ concentration to the photoactivity (seen in Fig. 1B and C). According to the results of Fig. 1B and C, the composites photoactivity both showed rising first and falling later with the increase of g-C₃N₄ content and 20%g-C₃N₄-TiO₂-400 and

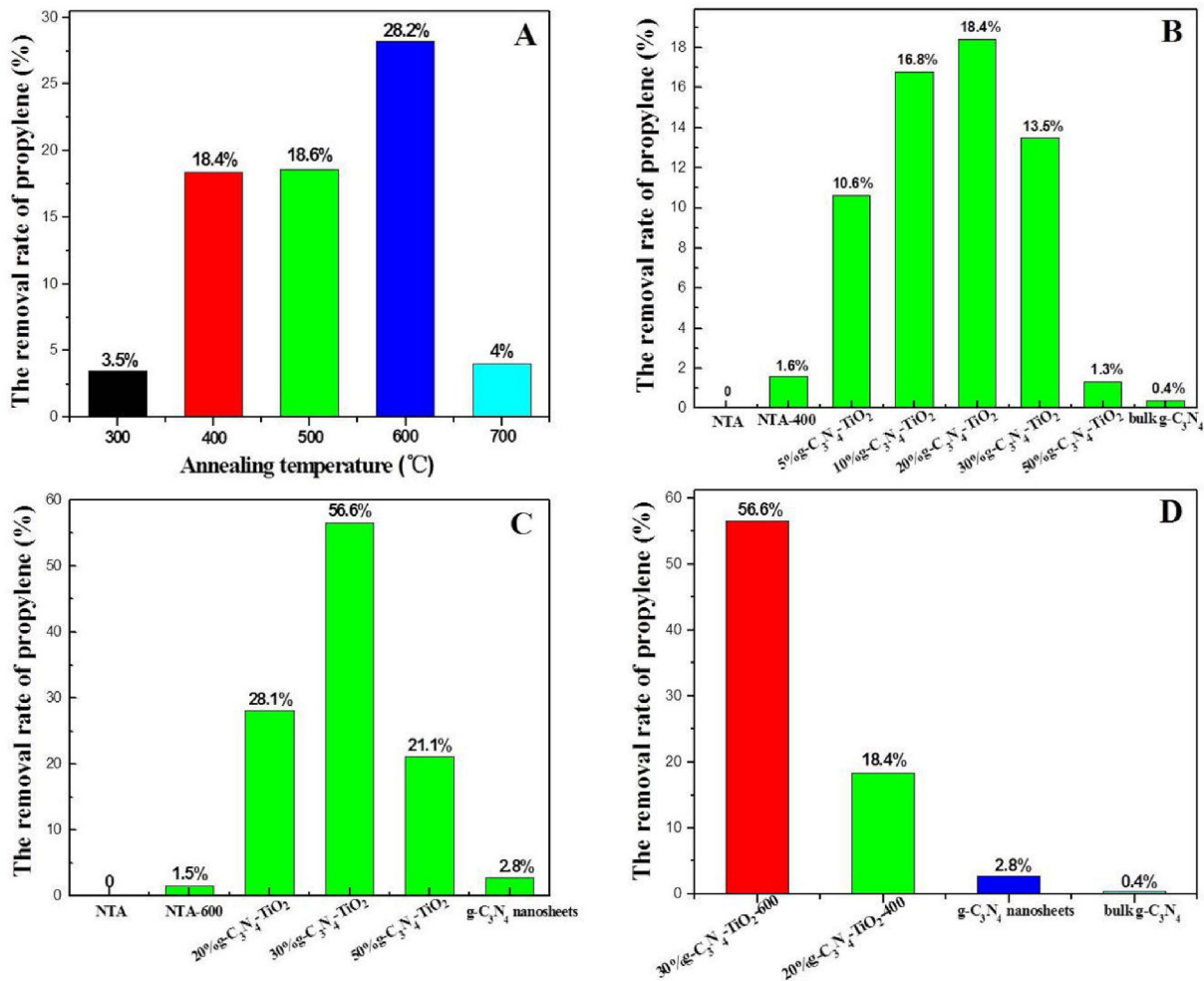


Fig. 1. Photocatalytic activity of various as-prepared photocatalysts for the photo-oxidation of propylene under visible light ($\lambda \geq 420$ nm) illumination: (A) 20% g-C₃N₄-TiO₂ obtained at different annealing temperatures, (B) g-C₃N₄-TiO₂-400 composites with different content of g-C₃N₄, (C) g-C₃N₄-TiO₂-600 composites with different content of g-C₃N₄, (D) 20%g-C₃N₄-TiO₂-400 and 30%g-C₃N₄-TiO₂-600 composites as well as bulk g-C₃N₄ and g-C₃N₄ nanosheets.

30%g-C₃N₄-TiO₂-600 were the optimum activity samples at 400 °C or 600 °C respectively.

Fig. 1D demonstrated that the activity of 30%g-C₃N₄-TiO₂-600 and 20%g-C₃N₄-TiO₂-400 for propylene oxidation were about 20 times and 6.6 times higher respectively than that of g-C₃N₄ nanosheets and the bulk g-C₃N₄ had the worst activity for the high electrons-holes recombination rate and the very small specific surface area (ca. 10m²/g, seen in Table S1). In addition, the results of hydrogen generation by water-splitting also showed that the activity of 30%g-C₃N₄-TiO₂-600 was twice than that of 20%g-C₃N₄-TiO₂-400 with loading 1%Pt under UV-vis light or visible light illumination (seen in Fig. S1).

On the basis of above analysis, we selected the samples with the optimum photocatalytic activity at 400 and 600 °C respectively to investigate the reason for the vast difference of activity. The specific reason would be expounded in detail in the subsequent section.

3.2. Effect of the calcination temperature on the morphology and structure of the g-C₃N₄-TiO₂ composites

In order to make certain the large photoactivity difference between the two samples of 400 and 600 °C, we performed the tests of XRD, TEM and AFM. The low magnification and high resolution TEM images of 20%g-C₃N₄-TiO₂-400 and 30%g-C₃N₄-TiO₂-600 (seen in Fig. S2) indicated that TiO₂ nanoparticles exhibit irregular

morphology while g-C₃N₄ present sheet-like appearance. Besides, the two kinds of photocatalysts show clear lattice fringes of TiO₂ and g-C₃N₄, which demonstrates that TiO₂ and g-C₃N₄ are well integrated in the g-C₃N₄-TiO₂ composites. The crystal structure of the composites was determined by the method of X-ray diffraction as shown in Fig. 2A and B. It could be seen that there were two characteristic peaks corresponding to (100) and (002) lattice plane respectively in the bulk g-C₃N₄ and g-C₃N₄ nanosheets. However, it only showed the specific peaks of the anatase TiO₂ but the peaks of g-C₃N₄ were not observed or un conspicuous in the samples of 30%g-C₃N₄-TiO₂-600 and 20%g-C₃N₄-TiO₂-400. That should be due to the very low content of g-C₃N₄ in the composites (seen the TG results in Fig. S3). In order to discern the morphology of g-C₃N₄ in the composites of 400 and 600 °C, we calcined the samples of g-C₃N₄-400 and g-C₃N₄-600 by heating bulk g-C₃N₄ at 400 and 600 °C respectively. The effect of the calcination temperature on the morphology of g-C₃N₄ was shown in Fig. 2C and D. The bulk g-C₃N₄-400 showed the plane layered structure while g-C₃N₄-600 presented poly porous construction with curly edge arising from the minimality of the surface energy for g-C₃N₄ nanosheets. This indicated that the thickness of bulk g-C₃N₄-400 was thicker than that of g-C₃N₄-600. In addition, the AFM images in Fig. 2E and F demonstrated that the thickness of g-C₃N₄ nanosheets was about 5 nm and 4 nm in the samples of 400 and 600 °C respectively and diminished with the increase of annealing temperature. The imporous plane struc-

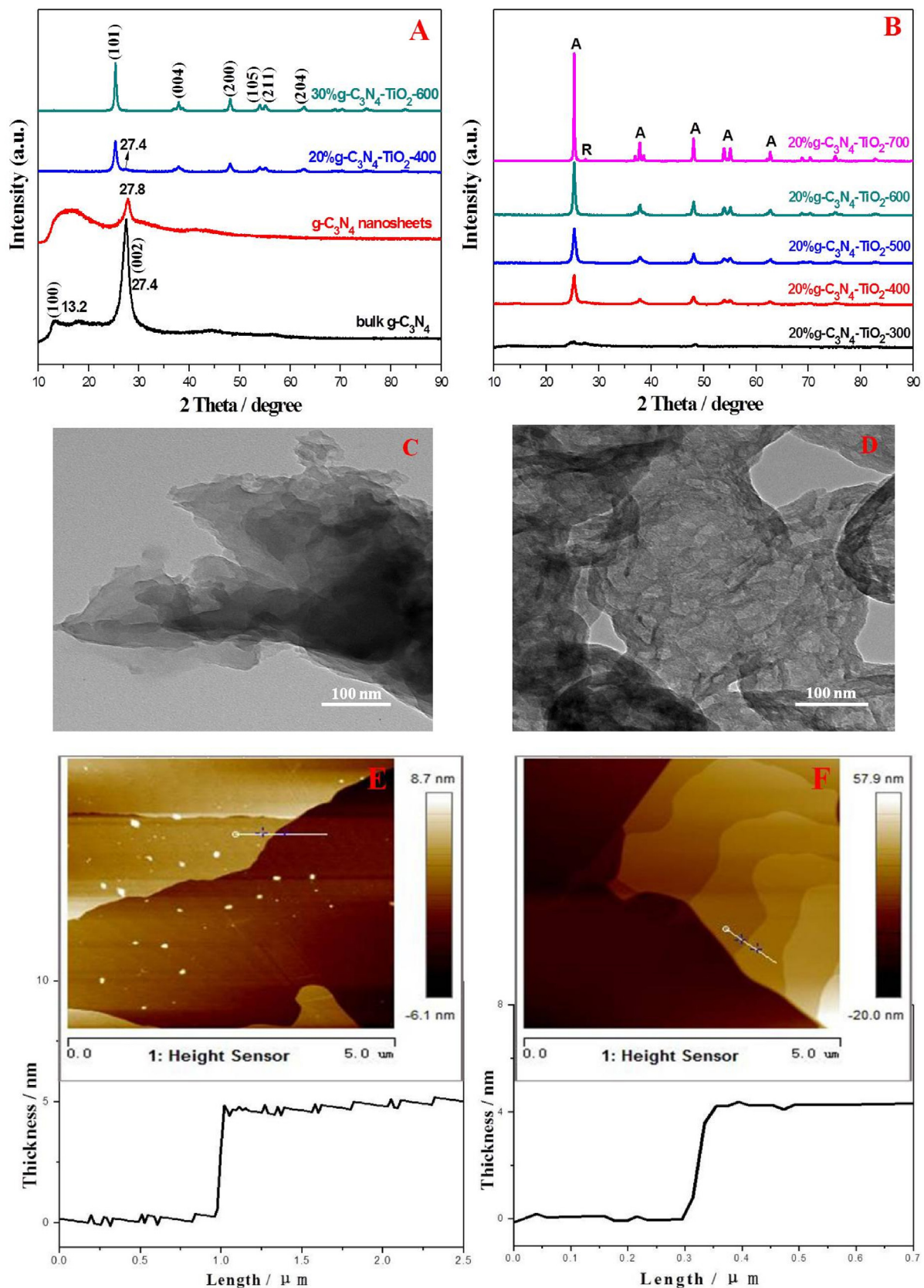


Fig. 2. XRD patterns of (A) the as-prepared photocatalysts and (B) samples in the 20% of $g\text{-C}_3\text{N}_4\text{-TiO}_2$ with different annealing temperature, TEM images of (C) $g\text{-C}_3\text{N}_4\text{-400}$ and (D) $g\text{-C}_3\text{N}_4\text{-600}$ and the AFM images of (E) $20\%g\text{-C}_3\text{N}_4\text{-TiO}_2\text{-400}$ and (F) $30\%g\text{-C}_3\text{N}_4\text{-TiO}_2\text{-600}$.

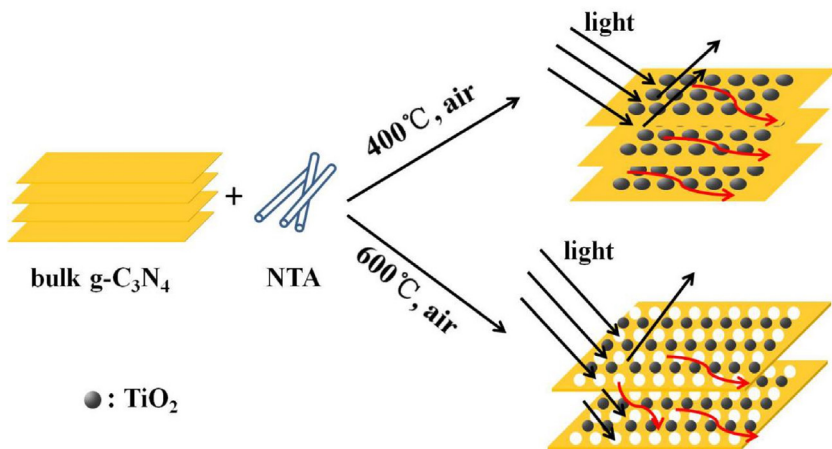


Fig. 3. The schematic diagram of the photocatalytic mechanism in $\text{g-C}_3\text{N}_4\text{-TiO}_2$ photocatalysts obtained by different calcination temperature treatment was proposed under visible light illumination.

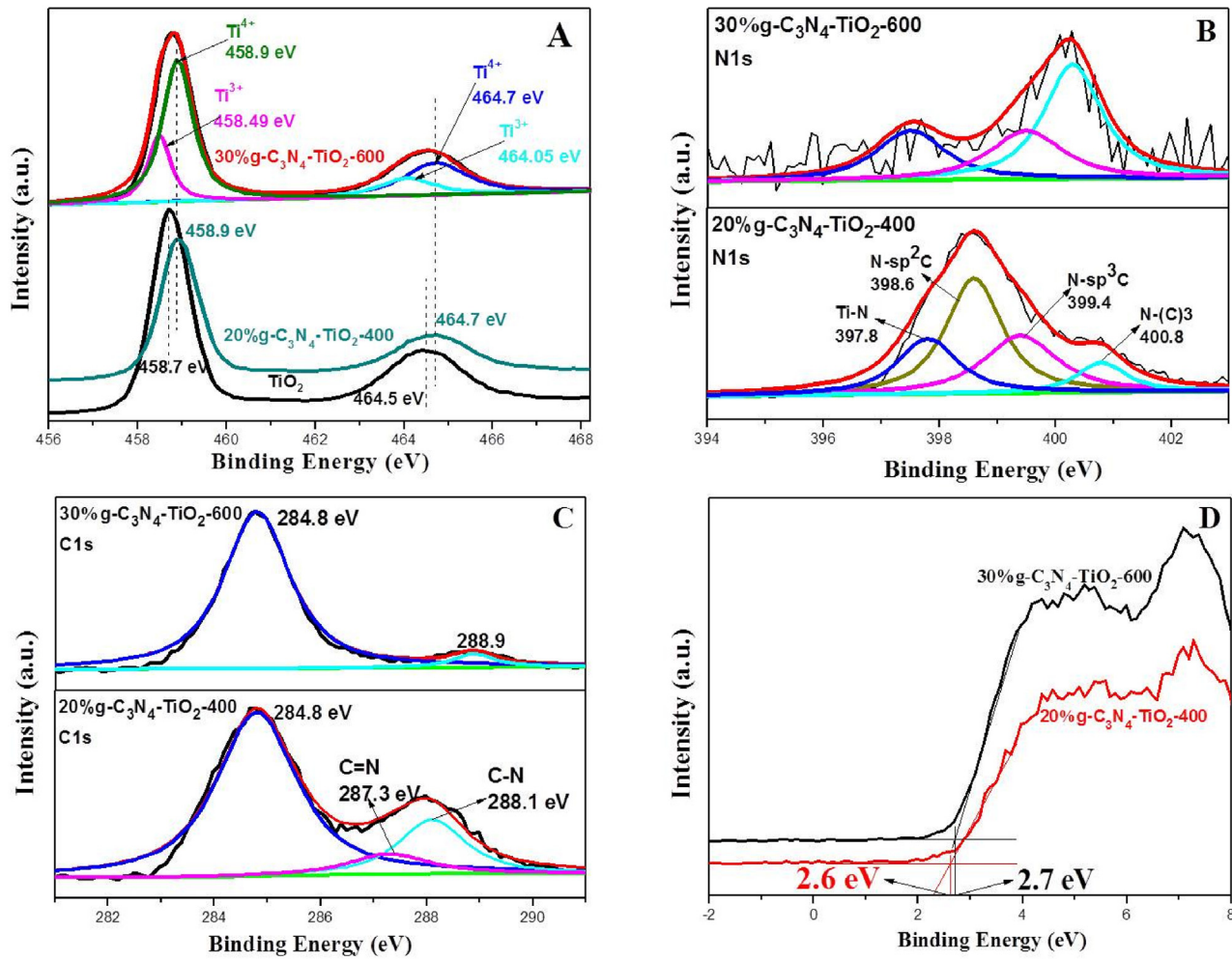


Fig. 4. High-resolution XPS spectra of (A) Ti2p, (B) N1s, (C) C1s, and (D) valence band spectra of $\text{g-C}_3\text{N}_4\text{-TiO}_2$ samples.

ture made the transfer of photoinduced carrier only along in-plane direction while the thinner and porous $\text{g-C}_3\text{N}_4$ nanosheets usually provided plentiful exposed surfaces, numerous active sites, a short transport length for increasing the separation efficiency of interface photoexcited carrier [30–32] and the more irradiation of the incident light. This might explain why 30% $\text{g-C}_3\text{N}_4\text{-TiO}_2$ -600 sample had the much higher activity than 20% $\text{g-C}_3\text{N}_4\text{-TiO}_2$ -400 (schematic diagram seen in Fig. 3).

XPS spectra were utilized to analysis the elemental composition and discern the chemical state of elements in $\text{g-C}_3\text{N}_4\text{-TiO}_2$ nanocomposites. From the results of Fig. S5, it could be inferred that there were only four elements in the composites although the intensity of N element in the sample of 30% $\text{g-C}_3\text{N}_4\text{-TiO}_2$ -600 was very weak. It should be attributed to the very little retained N atoms in the thermal oxidation treatment process [30,33]. Fig. 4A was the comparison data of the XPS Ti 2p spectra of TiO_2 ,

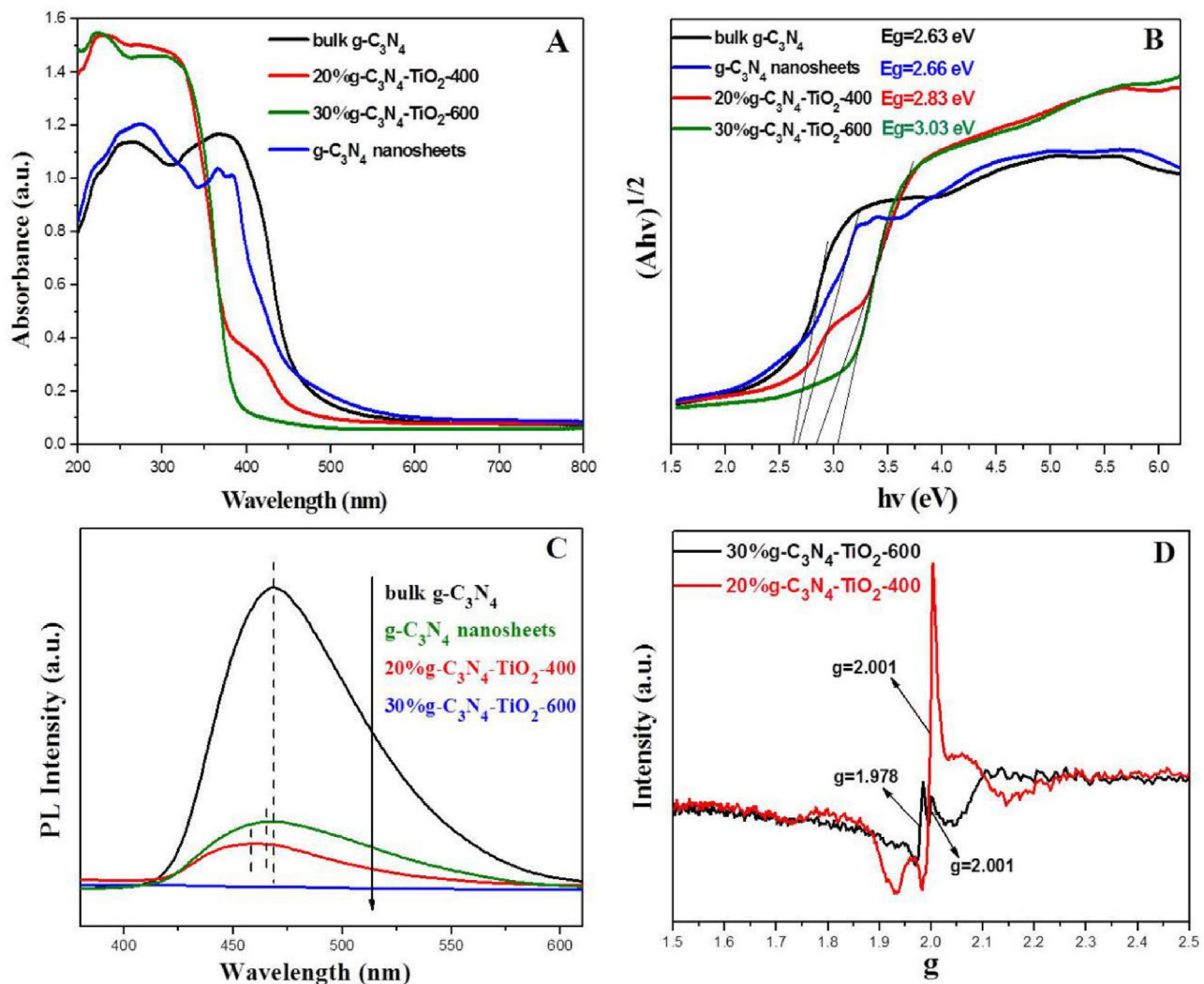


Fig. 5. (A) UV-vis diffuse reflectance spectra, (B) The plots of transformed Kubelka-Munk functions versus the light energy, (C) The fluorescence emission spectra of the as-prepared samples and (D) ESR spectra of 30%g-C₃N₄-TiO₂-600 and 20%g-C₃N₄-TiO₂-400 samples measured at room temperature in air.

20%g-C₃N₄-TiO₂-400 and 30%g-C₃N₄-TiO₂-600. The Ti 2p peak of 30%g-C₃N₄-TiO₂-600 can be divided into four peaks; and in particular, the peaks at 458.49 eV and 464.05 eV can be assigned to Ti³⁺ 2p_{3/2} and Ti³⁺ 2p_{1/2}, which gives evidences to the existence of Ti³⁺ in 30%g-C₃N₄-TiO₂-600. Moreover, as compared with that of commercial TiO₂, the Ti 2p peaks of 20%g-C₃N₄-TiO₂-400 and 30%g-C₃N₄-TiO₂-600 tend to shift towards higher binding energy by about 0.2 eV, possibly due to the interaction between TiO₂ and g-C₃N₄ [27].

According to the comparison of N1s spectra of the samples obtained at 400 °C and 600 °C (seen in Fig. 4B), there were four N1s signal peaks located at about 397.8, 398.6, 399.4 and 400.8 eV corresponding to Ti-N bond, pyridine-like (N-sp²C) nitrogen, pyrrole-like (N-sp³C) nitrogen and graphitic nitrogen respectively [36,37] in the sample of 20%g-C₃N₄-TiO₂-400. While the peak of pyridine-like (N-sp²C) nitrogen located at 398.6 eV disappeared and the intensity of graphitic nitrogen peak obviously increased in 30%g-C₃N₄-TiO₂-600 sample. That indicated that pyridine-like nitrogen would transform into graphitic nitrogen when the annealing temperature exceeded the decomposition temperature of g-C₃N₄. Fig. 4B also illustrated that pyridine-like nitrogen was the main component in the samples of 20%g-C₃N₄-TiO₂-400, while the graphitic nitrogen was the main N species in the sample obtained at 600 °C.

Furthermore, from the C1s spectra (Fig. 4C), it could be observed that the peak of 287.3 eV (C=N) in the sample of 30%g-C₃N₄-TiO₂-600 disappeared and the peak of 288.1 eV (C—N, namely three coordination C, denoted as C_{3c}) shifted to 288.9 eV (two coordination C_{2c} transformed from C_{3c}) comparison with that of 20%g-C₃N₄-TiO₂-400 sample. The reason was that pyridine-like (N-sp²C) nitrogen was two coordination and easily be oxidized to break [30,38] and result in the formation of C_{2c} in the thermal treatment. According to the literature [36], the graphitic nitrogen was favorable to form the π-conjugated system and that was beneficial to the carriers transport. Namely, 30%g-C₃N₄-TiO₂-600 exhibits a larger positive valence band potential than 20%g-C₃N₄-TiO₂-400 (see Fig. 4D), which is why it exhibits better oxidation ability and photocatalytic activity than the latter.

3.3. The photophysical behaviors of photoexcited carriers of the samples

The photophysical behaviors of photogenerated charge carriers in the samples were analyzed by combining UV-vis diffuse reflectance spectrometry (denoted UV-vis DRS) with fluorescence emission spectra. UV-vis DRS was generally used for illustrating the strength of light absorption ability. As shown from Fig. 5A, all the samples possessed the excellent visible light absorption

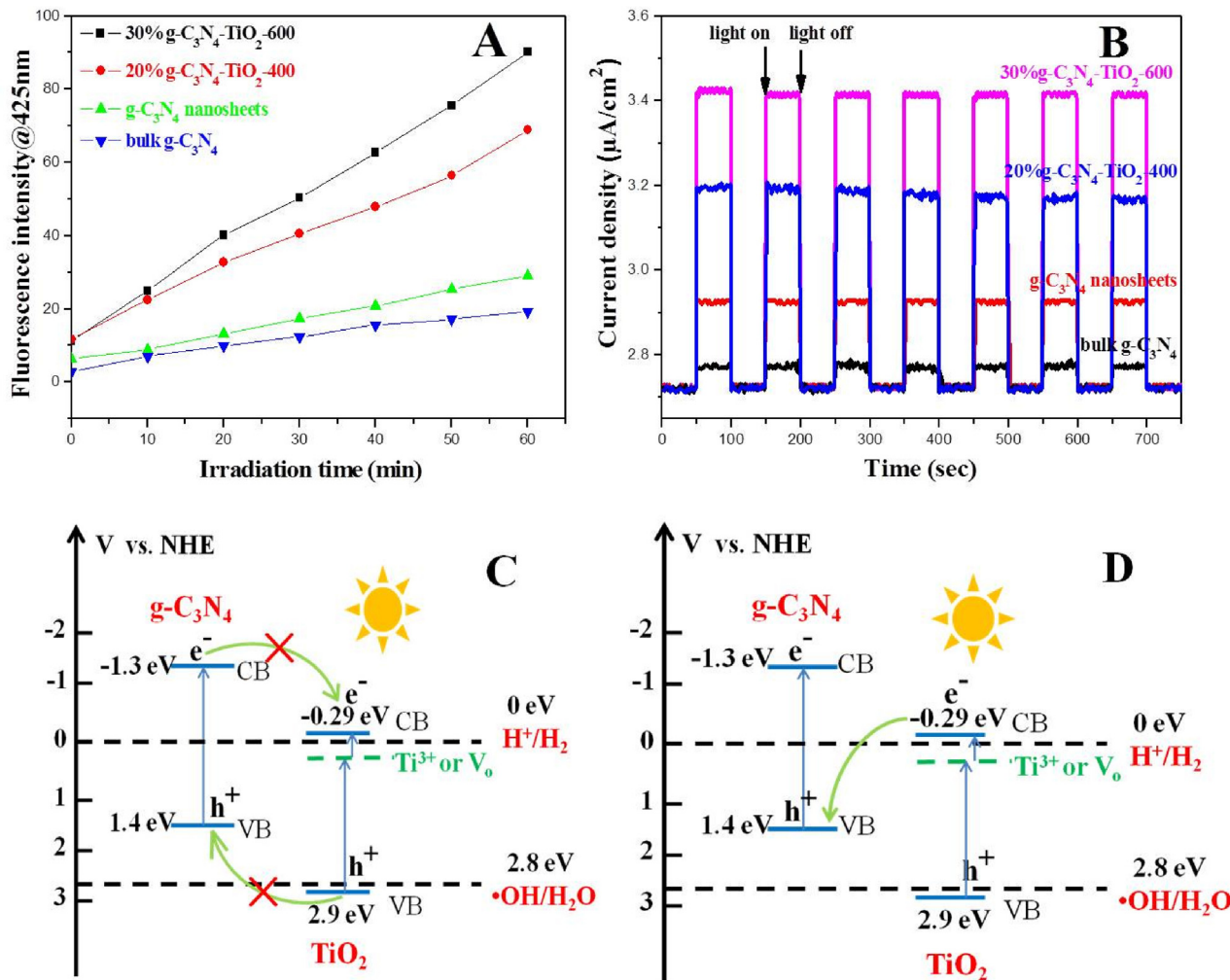


Fig. 6. (A) The samples of PL intensity@425 nm in 2×10^{-3} M NaOH solution with presence of 5×10^{-4} M terephthalic acid, (B) Photocurrent-time curves of the investigated photocatalysts at certain interval time under visible light ($\lambda \geq 420$ nm) irradiation and the photocatalytic mechanism diagram of (C) traditional heterojunction and (D) Z-scheme construction in the sample of g-C₃N₄-TiO₂.

ability at 390–600 nm except for the sample of 30%g-C₃N₄-TiO₂-600. Fig. 5B was the curves of the converted by Kubelka-Munk (KM) functions as the function of light energy of the investigated samples. According to Fig. 5B, the estimated bandgaps were 2.63, 2.66, 2.83 and 3.03 eV corresponding to the samples of bulk g-C₃N₄, g-C₃N₄ nanosheets, 20%g-C₃N₄-TiO₂-400 and 30%g-C₃N₄-TiO₂-600, respectively. The bandgap of g-C₃N₄ nanosheets was increased by 0.03 eV than that of bulk g-C₃N₄ which should be due to the quantum confinement effect. Moreover, the bandgap of 20%g-C₃N₄-TiO₂-400 and 30%g-C₃N₄-TiO₂-600 is decreased by 0.37 eV and 0.17 eV as compared with that of anatase TiO₂ (3.2 eV), which implies that 20%g-C₃N₄-TiO₂-400 and 30%g-C₃N₄-TiO₂-600 could exhibit higher light absorption efficiency than the commercial anatase TiO₂.

Usually, the larger specific surface areas and the stronger UV-vis light absorption ability could result in the better photocatalytic effect because of the more reaction active sites and photogenerated carriers. However, an increased light absorption ability of photocatalysts does not always mean an increased photocatalytic activity, unless the photocatalysts possess a low enough photoexcited electron-hole recombination rate. That was the reason why 20%g-C₃N₄-TiO₂-400 sample had the larger specific surface areas (seen in Fig. S4 and Table S1) and the better visible light absorption (seen in Fig. 5A) but had the worse photocatalytic activity than that

of 30%g-C₃N₄-TiO₂-600 sample. So the high charge separation and transfer efficiency were the key factors for improving the activity.

According to the fluorescence peak intensity in the fluorescence emission spectra of a catalyst, the charge separation and transfer efficiency could be estimated. Fig. 5C showed that the fluorescence intensity of g-C₃N₄ nanosheets, 20%g-C₃N₄-TiO₂-400 and 30%g-C₃N₄-TiO₂-600 decreased obviously compared with that of the bulk g-C₃N₄ which further indicated that the recombination rate of photogenerated electrons and holes decreased. The fluorescence emission peak of bulk g-C₃N₄ located at about 470 nm corresponding to the bandgap of 2.63 eV and the fluorescence emission peak position of g-C₃N₄ nanosheets, 20%g-C₃N₄-TiO₂-400 and 30%g-C₃N₄-TiO₂-600 took place obvious blue shift which was consistent with the results of UV-vis diffuse reflectance spectra. This further indicated that the thickness of g-C₃N₄ nanosheets in the composites was decreased (seen in Fig. 2E and F), and which did favor for the transfer of the charge carriers, and leading to a higher photoactivity.

From the ESR results of Fig. 5D, 20%g-C₃N₄-TiO₂-400 sample only contained the signal of single-electron trapped oxygen vacancy (denoted as V_o[•], g=2.001), while 30%g-C₃N₄-TiO₂-600 sample possessed the signals of V_o[•] and g=1.978 which was assigned to the paramagnetic Ti³⁺ center [39]. The reason was that g-C₃N₄ would partially decompose and release reducing gas NH₃

Table 1

The best fitted parameters of time-resolved fluorescence decay spectra.

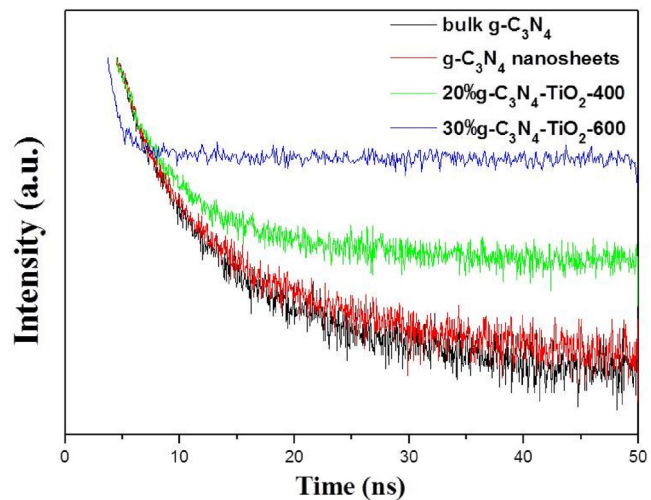
Sample	τ_1 (ns)-Rel%	τ_2 (ns)-Rel%	τ_3 (ns)-Rel%	Goodness of fit parameter (χ^2)
Bulk $\text{g-C}_3\text{N}_4$	2.048–39.98	9.009–60.02	–	1.070
$\text{g-C}_3\text{N}_4$ nanosheets	2.162–43.02	10.05–56.98	–	1.132
20% $\text{g-C}_3\text{N}_4$ - TiO_2 -400	1.535–19.62	4.103–44.49	17.23–35.9	1.073
30% $\text{g-C}_3\text{N}_4$ - TiO_2 -600	0.8084–54.61	11.96–45.39	–	1.190

at 600 °C in air which could reduce a part of Ti^{4+} to Ti^{3+} , as the evidence by relevant XPS Ti 2p spectra of 20% $\text{g-C}_3\text{N}_4$ - TiO_2 -400 and 30% $\text{g-C}_3\text{N}_4$ - TiO_2 -600. The emerging Ti^{3+} would become the segregated center of photoinduced carrier and enhance the separation efficiency [25], thus could improve the photocatalytic activity of the sample. In addition, as shown from Fig. 5D, the bulk V_0^\bullet concentration of 600 °C sample was far lower than that of 400 °C sample. In our previous work [35,40], V_0^\bullet usually was the recombination center of photo-generated e^- - h^+ , so the higher bulk V_0^\bullet concentration was harmful to the photocatalytic reaction.

3.4. Photocatalytic mechanism of $\text{g-C}_3\text{N}_4$ - TiO_2 heterojunction for propylene oxidation

In order to distinguish the photocatalytic mechanism was the Z-scheme structure (seen in Fig. 6D) or the traditional heterojunction construction (seen in Fig. 6C), the $\text{g-C}_3\text{N}_4$ - TiO_2 composites was carried out the test of capturing hydroxyl radical using terephthalic acid as probe molecule by fluorescence method. On account of terephthalic acid could only react with dissociative hydroxyl radical to form 2-hydroxyterephthalic acid and emit fluorescence at about 425 nm, the intensity of fluorescence peak at 425 nm could indicate the concentration of dissociative hydroxyl radical. Fig. 6A showed that both the two samples of 30% $\text{g-C}_3\text{N}_4$ - TiO_2 -600 and 20% $\text{g-C}_3\text{N}_4$ - TiO_2 -400 could generate large amounts of dissociative hydroxyl radical under visible light irradiation and 30% $\text{g-C}_3\text{N}_4$ - TiO_2 -600 possessed stronger ability of generating hydroxyl radical arising from its stronger oxidizability at valence band than that of 20% $\text{g-C}_3\text{N}_4$ - TiO_2 -400 (seen in Fig. 4D). While bulk $\text{g-C}_3\text{N}_4$ and $\text{g-C}_3\text{N}_4$ nanosheets could produce hydroxyl radical attributed to the reaction of OH^\bullet in the water with superoxide radical deriving from surface adsorption oxygen obtained conduction band electrons of $\text{g-C}_3\text{N}_4$. That indicated that the photo-oxidation mechanism of propylene by the $\text{g-C}_3\text{N}_4$ - TiO_2 heterojunction was the Z-scheme system, not the traditional heterojunction structure. The Z-scheme system can keep the stronger oxidation and reduction ability of the valence and conduction charge carriers, thereby resulting in increased photocatalytic activities.

To further inspect the separation ability of the photo-induced electrons and holes, we performed the photocurrent tests at an interval time with periodic visible light irradiation (as shown in Fig. 6B) and time-resolved fluorescence decay spectra measurement (seen in Fig. 7 and Table 1). Fig. 6B showed that the results of all the samples were consistent with their photoactivity; and in particular, 30% $\text{g-C}_3\text{N}_4$ - TiO_2 -600 exhibits the highest photocurrent density (corresponding to the best photoinduced charge separation ability). Fig. 7 indicated that all the curves presented exponential attenuation and $\text{g-C}_3\text{N}_4$ - TiO_2 composites decayed more slowly than that of the pure $\text{g-C}_3\text{N}_4$ which demonstrated the photoexcited charge carriers in the $\text{g-C}_3\text{N}_4$ - TiO_2 composites had the longer lifetime. More important, the high separation efficiency of photoexcited carriers rather than the high lifetime of the charge carriers plays a key role in terms of the photocatalytic activity of the as-prepared photocatalysts. Therefore, 30% $\text{g-C}_3\text{N}_4$ - TiO_2 -600 photocatalyst containing thin and porous plane structure could have promising potential in accelerating the photocatalytic degradation

**Fig. 7.** The time-resolved fluorescence decay spectra of as-prepared photocatalysts.

of organic pollutant like propylene, due to its ability to improve charge separation efficiency and facilitate fast carrier transport.

4. Conclusions

A series of $\text{g-C}_3\text{N}_4$ - TiO_2 direct contact Z-scheme heterojunction composites were prepared via simple annealing the mixture of NTA and bulk $\text{g-C}_3\text{N}_4$ at different temperatures and it was found that the temperature had significant impact to the photocatalytic activity of the composites. That was mainly due to the influence of calcination temperature to the structure of $\text{g-C}_3\text{N}_4$. Particularly, in association with the considerable decrease of the bulk V_0^\bullet concentration, the annealing at an appropriate temperature (e.g., 600 °C) affords Ti^{3+} with a good ability to separate photo-generated carrier. Therefore, $\text{g-C}_3\text{N}_4$ - TiO_2 -600 composite photocatalyst, without pyridine-like nitrogen and containing graphitic nitrogen as the major N species as well as thin-porous $\text{g-C}_3\text{N}_4$ nanosheet structure and Ti^{3+} , exhibits the best photocatalytic activity towards the visible light photocatalytic degradation of organic pollutant like propylene. Meanwhile, the hydrogen generation activity of $\text{g-C}_3\text{N}_4$ - TiO_2 -600 composites was about 2 times than that of $\text{g-C}_3\text{N}_4$ - TiO_2 -400 composites under UV-vis and visible light irradiation. This can be attributed to the polyporous construction of $\text{g-C}_3\text{N}_4$ nanosheets in the composites of 600 °C arising from the decomposition of $\text{g-C}_3\text{N}_4$, the more positive valence band potential resulted in stronger oxidizing ability. In summary, the direct Z-scheme heterojunction effect, in association with the desired charge transfer and separation efficiency between $\text{g-C}_3\text{N}_4$ nanosheets and novel TiO_2 , makes it feasible for $\text{g-C}_3\text{N}_4$ - TiO_2 -600 to be used as a promising photocatalyst for the degradation of organic pollutant like propylene under visible light irradiation.

Acknowledgments

The authors gratefully acknowledge the financial support provided by the National Natural Science Foundation of China (No.

21673066, 21103042), Program for Science & Technology Innovation Talents (No. 15HASTIT043) and Innovative Research Team (No. 16IRTSTHN015) from the Henan University of Henan Province. The authors would like to thank the help of Professor Laigui Yu for critically polishing the manuscript.

Appendix A. Supplementary data

Supplementary data associated with this article can be found, in the online version, at <http://dx.doi.org/10.1016/j.apcatb.2017.04.061>.

References

- [1] X. Chen, S.S. Mao, *Chem. Rev.* 107 (2007) 2891–2959.
- [2] M.R. Hoffmann, S.T. Martin, W. Choi, D.W. Bahneman, *Chem. Rev.* 95 (1995) 69–96.
- [3] A. Escudero, F. Langenhorst, *J. Solid State Chem.* 190 (2012) 61–67.
- [4] K. Bhattacharyya, J. Majeed, K.K. Dey, P. Ayyub, A.K. Tyagi, S.R. Bharadwaj, *J. Phys. Chem. C* 118 (2014) 15946–15962.
- [5] J. Yu, Q. Li, S. Liu, M. Jaroniec, *J. Chem. Eur.* 19 (2013) 2433–2441.
- [6] Y. Wang, C. Feng, M. Zhang, J. Yang, Z. Zhang, *Appl. Catal. B* 104 (2011) 268–274.
- [7] R. Asahi, T. Morikawa, T. Ohwaki, K. Aoki, Y. Taga, *Science* 293 (2001) 269–271.
- [8] Z. Zhang, S. Dai, M. Zhang, Y. Guo, J. Yang, *J. Electrochem. Soc.* 163 (2015) H42–H47.
- [9] H. Wei, Y. Wu, N. Lun, F. Zhao, *J. Mater. Sci.* 39 (2004) 1305–1308.
- [10] T. IHARA, M. MIYOSHI, *J. Mater. Sci.* (2001) 7.
- [11] J. Huo, Y. Hu, H. Jiang, C. Li, *Nanoscale* 6 (2014) 9078–9084.
- [12] J. Cai, Y. Wang, Y. Zhu, M. Wu, H. Zhang, X. Li, Z. Jiang, M. Meng, *ACS Appl. Mater. Interfaces* 7 (2015) 24987–24992.
- [13] Z.A. Huang, Q. Sun, K. Lv, Z. Zhang, M. Li, B. Li, *Appl. Catal. B* 164 (2015) 420–427.
- [14] J. Yu, S. Wang, J. Low, W. Xiao, *Phys. Chem. Chem. Phys.* 15 (2013) 16883–16890.
- [15] W.-K. Jo, T.S. Natarajan, *Chem. Eng. J.* 281 (2015) 549–565.
- [16] X. Wang, K. Maeda, A. Thomas, K. Takanabe, G. Xin, J.M. Carlsson, K. Domen, M. Antonietti, *Nat. Mater.* 8 (2009) 76–80.
- [17] W. Yu, D. Xu, T. Peng, *J. Mater. Chem. A* 3 (2015) 19936–19947.
- [18] J. Lv, K. Dai, J. Zhang, L. Geng, C. Liang, Q. Liu, G. Zhu, C. Chen, *Appl. Surf. Sci.* 358 (2015) 377–384.
- [19] X. Wang, S. Blechert, M. Antonietti, *ACS Catal.* 2 (2012) 1596–1606.
- [20] W.J. Ong, L.L. Tan, Y.H. Ng, S.T. Yong, S.P. Chai, *Chem. Rev.* 116 (2016) 7159–7329.
- [21] Y. He, J. Cai, T. Li, Y. Wu, H. Lin, L. Zhao, M. Luo, *Chem. Eng. J.* 215–216 (2013) 721–730.
- [22] T. Li, L. Zhao, Y. He, J. Cai, M. Luo, J. Lin, *Appl. Catal. B* 129 (2013) 255–263.
- [23] Y. Liu, R. Wang, Z. Yang, H. Du, Y. Jiang, C. Shen, K. Liang, A. Xu, *Chin. J. Catal.* 36 (2015) 2135–2144.
- [24] S. Kumar, A. Baruah, S. Tonda, B. Kumar, V. Shanker, B. Sreedhar, *Nanoscale* 6 (2014) 4830–4842.
- [25] K. Li, S. Gao, Q. Wang, H. Xu, Z. Wang, B. Huang, Y. Dai, J. Lu, *ACS Appl. Mater. Interfaces* 7 (2015) 9023–9030.
- [26] N. Yang, G. Li, W. Wang, X. Yang, W.F. Zhang, *J. Phys. Chem. Solids* 72 (2011) 1319–1324.
- [27] Q. Li, L. Zong, Y. Xing, X. Wang, L. Yu, J. Yang, *Sci. Adv. Mater.* 5 (2013) 1316–1322.
- [28] H. Yan, H. Yang, *J. Alloys Compd.* 509 (2011) L26–L29.
- [29] L. Shen, Z. Xing, J. Zou, Z. Li, X. Wu, Y. Zhang, Q. Zhu, S. Yang, W. Zhou, *Sci. Rep.* 7 (2017) 41978.
- [30] P. Niu, L. Zhang, G. Liu, H.-M. Cheng, *Adv. Funct. Mater.* 22 (2012) 4763–4770.
- [31] S. Yang, Y. Gong, J. Zhang, L. Zhan, L. Ma, Z. Fang, R. Vajtai, X. Wang, P.M. Ajayan, *Adv. Mater.* 25 (2013) 2452–2456.
- [32] Q. Lin, L. Li, S. Liang, M. Liu, J. Bi, L. Wu, *Appl. Catal. B* 163 (2015) 135–142.
- [33] J. Li, M. Zhang, Q. Li, J. Yang, *Appl. Surf. Sci.* 391 (2017) 184–193.
- [34] H. Li, F. Ren, J. Liu, Q. Wang, Q. Li, J. Yang, Y. Wang, *Appl. Catal. B* 172–173 (2015) 37–45.
- [35] M. Zhang, Z. Jin, J. Zhang, X. Guo, J. Yang, W. Li, X. Wang, Z. Zhang, *J. Mol. Catal. A: Chem.* 217 (2004) 203–210.
- [36] Z. Sheng, L. Shao, J. Chen, W. Bao, F. Wang, X. Xia, *ACS Nano* 5 (2011) 4350–4358.
- [37] Y. Li, H. Zhang, P. Liu, D. Wang, Y. Li, H. Zhao, *Small* 9 (2013) 3336–3344.
- [38] P. Niu, G. Liu, H.-M. Cheng, *J. Phys. Chem. C* 116 (2012) 11013–11018.
- [39] F. Zuo, L. Wang, T. Wu, Z. Zhang, D. Borchardt, P. Feng, *J. Am. Chem. Soc.* 132 (2010) 2.
- [40] J. Li, M. Zhang, Z. Guan, Q. Li, C. He, J. Yang, *Appl. Catal. B* 206 (2017) 300–307.